Medical Engineering and Physics 65 (2019) 8–23

Contents lists available at ScienceDirect

Medical Engineering and Physics

journal homepage: www.elsevier.com/locate/medengphy

# Study of the effect of stenosis severity and non-Newtonian viscosity on multidirectional wall shear stress and flow disturbances in the carotid artery using particle image velocimetry

Amanda L. DiCarlo[a], David W. Holdsworth[b,c,d,e], Tamie L. Poepping[a,b,*]

[a] Department of Physics and Astronomy, University of Western Ontario, 1151 Richmond Street, London, N6A 3K7 ON, Canada
[b] Department of Medical Biophysics, University of Western Ontario, 1151 Richmond Street, London, N6A 5C1 ON, Canada
[c] Department of Surgery, University of Western Ontario, 268 Grosvenor Street, London, N6A 4V2 ON, Canada
[d] Robarts Research Institute, University of Western Ontario, 1151 Richmond Street, London, N6A 5B7 ON, Canada
[e] Bone and Joint Institute, University of Western Ontario, 1151 Richmond Street, London, N6G 2V4 ON, Canada

ARTICLE INFO

*Article history:*
Received 3 March 2018
Revised 15 September 2018
Accepted 16 December 2018

*Keywords:*
Non-Newtonian fluid
Atherosclerosis
Stenosis severity
Carotid bifurcation
Wall shear stress
Oscillatory shear index
Transverse wall shear stress
Turbulence intensity
Stereoscopic particle image velocimetry
Shear-thinning
Blood analogue fluid

## ABSTRACT

The development of atherosclerosis at the carotid bifurcation is impacted by local variations in wall shear stress (WSS) magnitude and direction, as well as flow complexity within the vessel. In this study, stereoscopic particle image velocimetry (PIV) was used to investigate multidirectional WSS and disturbed flow for idealized models of the carotid bifurcation with varying eccentric stenosis of the internal carotid artery (ICA) and both Newtonian (N-fluid) and non-Newtonian (nN-fluid) blood analogues. Turbulence intensity (TI) was reduced with the nN-fluid compared to N-fluid for mild to moderate stenosis, and comparable for more severely stenosed (70%) models. Differences in maximum TI due to viscosity model ranged from 0.02 m/s to 0.06 m/s compared to much larger differences due to geometry of up to 0.29 m/s between mild and severe stenosis. The level of time-averaged WSS (TAWSS) increased with stenosis severity from 5 Pa to 32 Pa, and nN-fluid led to higher WSS on average than N-fluid counterparts. Regions of elevated oscillatory shear index (OSI) demarcated recirculation regions, and mean OSI in the ICA branch was reduced for nN-fluid models by 9–19% compared to N-fluid. Transverse WSS (transWSS) increased with WSS magnitude and again was higher in nN-fluid models. Surface area exposure to shear metrics indicated that a Newtonian viscosity assumption predicted larger regions of low and oscillatory WSS, while predicting reduced regions of high transWSS, in comparison to the more physiological shear thinning fluid.

## 1. Introduction

Atherosclerosis – a thickening and hardening of blood vessels due to endothelial dysfunction and plaque build-up - is one of the main risk factors for ischemic stroke and often develops at regions of complex flow patterns such as bifurcations. The focal development of atherosclerosis at particular sites in the arterial tree suggests that hemodynamic forces impact the initiation and progression of vascular disease. Specifically, in the carotid bifurcation, intimal thickening is greater at the outer wall of the carotid bulb opposite the flow divider, where low magnitude flow recirculation occurs [1]. Atherosclerosis has been shown to preferentially develop in regions of low and oscillatory shear stress [2–4] whereas regions with non-disturbed flow and steady, moderate to high shear levels exhibit atheroprotective genes. Furthermore, high wall shear stress (WSS), often found at the proximal side of existing plaques, may be linked to plaque vulnerability. More recently, endothelial cell sensing of flow and shear *directionality* have been shown to play a key role in endothelial cell pro-inflammatory responses [5–7].

Local variation in wall shear stress is often quantified in numerical and experimental studies using the oscillatory shear index (OSI), a metric first proposed by Ku et al. [8] to account for changes in the direction of the cycle-averaged shear stress vector under pulsatile flow. However, recent work failing to find

---

*Abbreviations:* CCA, common carotid artery; CFD, computational fluid dynamics; CT, computed tomography; ECA, external carotid artery; ICA, internal carotid artery; MRI, magnetic resonance imaging; N-fluid, Newtonian fluid; nN-fluid, non-Newtonian fluid; OSI, oscillatory shear index; PIV, particle image velocimetry; ROI, region of interest; TAWSS, time-averaged wall shear stress; TI, turbulence intensity; transWSS, transverse wall shear stress; WSS, wall shear stress; DUS, Doppler ultrasound.

[*] Corresponding author at: Department of Physics and Astronomy, University of Western Ontario, 1151 Richmond Street, London, N6A 3K7 ON, Canada.

*E-mail addresses:* adicarl3@uwo.ca (A.L. DiCarlo), poepping@uwo.ca (T.L. Poepping).

https://doi.org/10.1016/j.medengphy.2018.12.023
1350-4533/

definitive evidence for the low and/or oscillatory shear hypothesis [9,10] prompted the development of new metrics to quantify specifically the multi-directionality of WSS in arterial flows [6,7,11,12]. The traditional OSI parameter becomes ambiguous in distinguishing between uniaxially reversing shear and truly multi-directional shear stress [7]. Peiffer et al. [7] proposed the transverse wall shear stress (transWSS) metric to capture the flow multi-directionality and showed a qualitative association between transWSS modeled using CFD and regions of lipid deposition in the rabbit aorta. Additional shear metrics incorporating projections of the WSS along axial and orthogonal-to-axial directions [11,12] as well as normalization of the instantaneous transWSS components [13] have also been explored.

For a complete three-dimensional analysis of WSS magnitude and direction, it is a requirement to have both three-dimensional, three-component velocity vector data, as well as accurate three-dimensional wall-location information. This requirement is inherently met for numerical simulations but is more challenging to implement experimentally. In vivo hemodynamic studies are completed using either Doppler ultrasound (DUS) or phase-contrast magnetic resonance imaging (PC-MRI). The ability to calculate full three-dimensional maps of WSS from PC-MRI has been demonstrated, employing interpolation of the velocity field along the inward normal of a segmented vessel surface [14–18]. The use of MRI benefits from being able to capture both velocity data and vessel geometry in the same reference frame, eliminating registration steps, and also allowing patient-specific studies that correlate shear metrics directly with plaque localization [19,20]. However, MRI wall-shear estimates are limited by poor temporal and spatial resolution and highly influenced by errors in wall segmentation and thus also the estimated wall position. In addition, errors in WSS derived from MRI increase with shear magnitude, making MRI techniques less suitable in regions with high shear such as at a stenosis [21,22].

Particle image velocimetry (PIV) is a well-established technique for mapping velocity fields in vitro, and it has commonly been used to calculate WSS from 2D and 3D studies of various arterial geometries [23–25]. Buchmann et al. [26] used stereoscopic and tomographic PIV in combination with a computed tomography scan of the phantom vessel to compute 3D WSS magnitude over the vessel surface in a carotid artery model under steady inlet flow (i.e. non-pulsatile). However, their method only allowed the magnitude of the WSS to be calculated, thus any further investigation of directional shear metrics was not conducted. Previously, Kefayati et al. [27] used a similar method to calculate wall-shear magnitude in vessels of varying plaque stenosis severity and eccentricity under pulsatile flow with a Newtonian viscosity blood-analogue to assess spatial and temporal variations in velocities and WSS, but variation in shear direction was not explored.

Traditionally, experimental and numerical models of blood flow have assumed blood to be a Newtonian fluid with constant viscosity giving a linear stress–strain relationship, where the viscosity is approximated using the high-shear rate viscosity limit. However, blood viscosity characterization has shown that aggregation of red blood cells into long structures known as rouleaux causes the viscosity to increase in low-shear regions, and a shear-thinning behavior is observed. Approximating blood to be a Newtonian fluid may be acceptable at high shear rates in large arteries but may cause WSS measurements to be inaccurate in regions of low shear, as observed in the post-stenotic recirculation and regions of destabilized flow. Therefore, it would be beneficial to determine the effect of a Newtonian blood approximation when estimating local multidirectional shear patterns. Previous numerical studies have shown that a non-Newtonian viscosity model leads to flattened velocity profiles and longer recirculation zones compared to Newtonian, and that a Newtonian viscosity assumption underestimates WSS in low-shear stress regions due to the absence of shear-thinning behavior [28–30].

The objective of the present study is to utilize a multi-plane stereoscopic PIV system to obtain three-dimensional, three-component velocity vector fields and subsequently combine the dataset with geometry data segmented from micro-computed tomography images to calculate multi-directional WSS. Additionally, a shear-thinning blood analogue fluid was developed, with viscosity fit to a cross model [31], and results compared to a typical Newtonian blood-analogue fluid. Measurements were carried out in idealized carotid bifurcation models with varying stenosis of the internal carotid artery and under pulsatile flow conditions. The differences between modeling blood as either a Newtonian or non-Newtonian fluid when investigating disturbed flow, WSS, OSI and transWSS will be presented in diseased models displaying a broad range of physiological flow disturbances.

## 2. Methods

### 2.1. Flow set-up

Flow measurements were carried out in transparent, life-sized, PIV-compatible carotid bifurcation phantoms fabricated in polydimethylsiloxane (PDMS) using a lost-core casting technique [32] as employed in previous US and PIV studies [27,33–35]. Three idealized carotid geometries previously described by Smith et al. [36] and shown in Figure 1 were investigated, with common carotid artery (CCA) diameter of 8 mm and eccentric stenosis of the internal carotid artery (ICA) of 30%, 50%, and 70% based on NASCET criteria [37].

A computer-controlled positive-displacement pump (CompuFlow 1000, Shelley Medical Imaging Technologies, London ON Canada) was used to generate physiological pulsatile flow. An idealized carotid artery waveform based on in-vivo US measurements in young adults was applied at the CCA inlet [38]. Downstream flow resistors composed of small-diameter tubing create a physiologically realistic ICA:ECA flow division of 60:40 [33]. Flow and pressure waveforms were monitored at the phantom inlets and outlets using inline electromagnetic flowmeters (Model 501D, Carolina Medical Electronics, East Bend NC, USA) and a catheter-based pressure transducer (Model SPR-350S, Millar Inc., Houston, TX, USA). The measured CCA-inlet flow waveforms for all phantoms and blood analogue fluids are shown in Figure 2(a).

### 2.2. Blood analogue fluids

Two custom blood-analogue fluids were utilized, as previously optimized for use in PIV experiments with PDMS phantoms [31,39]. The first, previously applied in PIV experiments [27,34,35] is a Newtonian fluid (N-fluid) composed of water, glycerol and sodium iodide with a viscosity of 4.31 cP matching the high shear-rate viscosity range of human blood. The second includes the addition of xanthan gum to produce a non-Newtonian fluid (nN-fluid) whose composition is based on a best-match to blood viscosity data from a collection of ex vivo studies [40–45], as previously described [31]. The fluid formulations are given in Table 1.

The shear-dependent viscosity of the working fluid was measured using a couette-cell rheometer (MCR 302, Anton-Paar, Montreal QC, Canada) and a Cross model fit was applied for shear rates $>1$ s$^{-1}$ using non-linear least squares regression for use in WSS calculations. The Cross model of viscosity is given by

$$\eta(\dot{\gamma}) = \eta_\infty + \frac{\eta_0 - \eta_\infty}{1 + a\dot{\gamma}^{1-q}} \quad (1)$$

where $\eta_0$ and $\eta_\infty$ refer to the viscosities as shear rate, $\dot{\gamma}$, approaches zero and infinity, respectively, and $a$ and $q$ are constants

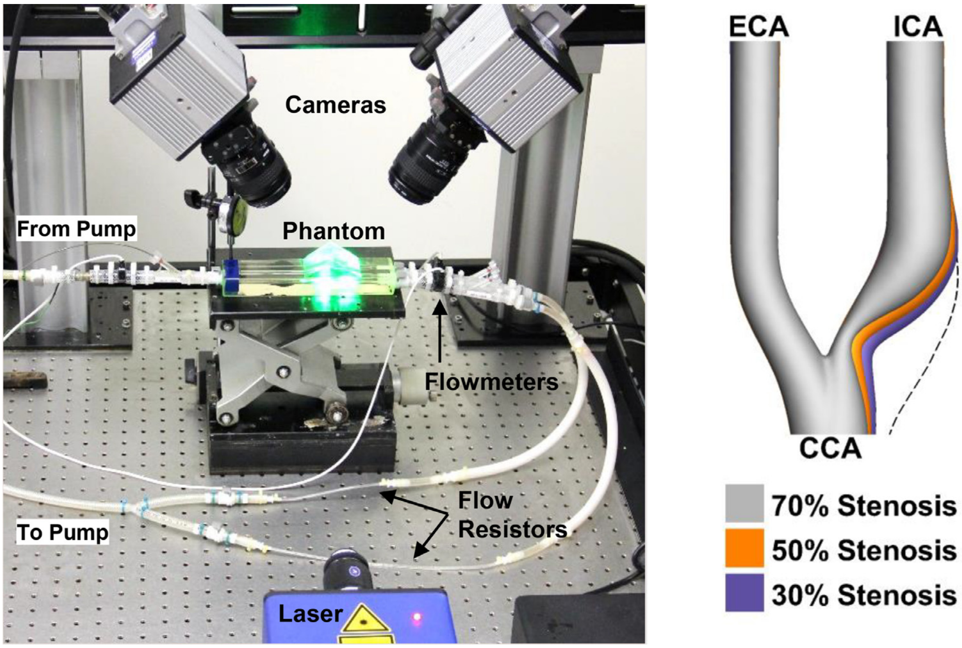

**Figure 1.** Experimental set-up including flow circuit and PIV components (left). Family of carotid artery bifurcation geometries with progressing degrees of eccentric stenosis (right). Dashed contour line indicates the boundary of the normal, disease-free geometry. CCA: common carotid artery, ICA: internal carotid artery, ECA: external carotid artery.

**Table 1**
Blood analogue fluid formulations.

| Blood analogue fluid | N-fluid | nN-fluid |
|---|---|---|
| Water (% w/w) | 47.4 | 51.9 |
| Glycerol (% w/w) | 36.9 | 22.2 |
| NaI (%w/w) | 15.7 | 25.9 |
| Xanthan gum (% w/w) | | 0.0019 |

determining the degree and rate of shear thinning. The measured viscosity data for the nN-fluid and the Cross model fit are shown in Figure 2(b) along with the literature blood data.

### 2.3. PIV data acquisition and velocity vector processing

The PIV image data were acquired using a commercial stereoscopic PIV system as shown in Figure 1. (LaVision Inc., Ypsilanti MI, USA). Double-frame images were acquired at 100 Hz (10 ms resolution) for 870 ms of the total 920 ms cardiac cycle, leaving 50 ms to prepare for the next pump synchronization pulse. The interframe time, dt, ranged from 100–250 µs, depending on the peak systolic velocity expected for a given stenosed model. Volumetric data were assembled by translating the phantom vertically in increments of 0.5 mm to collect 15 2D slices.

PIV data were processed (DaVis 7.2, LaVision Inc.) using a fast-Fourier-transform based cross-correlation algorithm with decreasing window size from 64 × 64 pixels to 16 × 16 pixels and 50% window overlap. For final passes, a Gaussian-window weighting and a high-accuracy Whittaker reconstruction was applied. This resulted in an in-plane vector spacing of approximately 0.3 mm across all models. Velocity maps were post-processed using a median filter to remove spurious vectors and one pass with a 3 × 3 smoothing kernel, and then stacked together to construct the 3D three-component velocity dataset.

### 2.4. Computed tomography imaging

A segmentation of the phantom geometry for WSS estimation was derived from computed tomography scans obtained using a volumetric cone-beam micro-CT scanner (Locus Ultra, General Electric Healthcare, London, ON, Canada). Surface data were obtained from the reconstructed CT images using a level-set segmentation method in the Vascular Modeling Toolkit (VMTK) [46]. Subsequent smoothing and remeshing steps were applied to achieve a coarse surface mesh of triangular elements with a mean edge length of 0.41 ± 0.06 µm across all models. The segmented lumen surface for each phantom was then registered to the respective volumetric PIV data using an iterative closest-point algorithm (VMTK) to the outermost velocity vectors nearest the wall. The registered vessel surface was cropped to include 8 mm proximal and 32 mm distal to the bifurcation apex for WSS calculation, resulting in a mean of 18,000 ± 500 surface elements per model.

### 2.5. Data analysis

#### 2.5.1. Wall shear stress

The formula for the Cauchy stress tensor is

$$\boldsymbol{\sigma} = -p\boldsymbol{I} + \boldsymbol{\tau} \tag{2}$$

where $p$ is the pressure, $\boldsymbol{I}$ is the identity matrix and $\boldsymbol{\tau}$ is the deviatoric stress tensor representing the viscous stresses. For an incompressible, Newtonian fluid the deviatoric stress tensor $\boldsymbol{\tau}$ is given by

$$\boldsymbol{\tau} = \eta\dot{\boldsymbol{\gamma}} = \eta\left(\nabla\boldsymbol{u} + (\nabla\boldsymbol{u})^T\right) \tag{3}$$

where $\dot{\boldsymbol{\gamma}}$ is the symmetric rate-of-strain tensor. The deviatoric stress tensor for a Newtonian fluid becomes, using tensor notation,

$$\tau_{ij} = \eta\left(\frac{\partial u_i}{\partial x_j} + \frac{\partial u_j}{\partial x_i}\right) \tag{4}$$

The traction vector at a specific surface point is given by the dot product of the stress tensor with the surface inward normal vector, $\boldsymbol{N}$:

$$\boldsymbol{t} = \boldsymbol{N} \cdot \boldsymbol{\tau} \tag{5}$$

Finally, the component of the traction vector tangential to the vessel wall is denoted the wall shear stress vector.

$$\boldsymbol{\tau_w} = \boldsymbol{t} - (\boldsymbol{t} \cdot \boldsymbol{N})\boldsymbol{N} \tag{6}$$

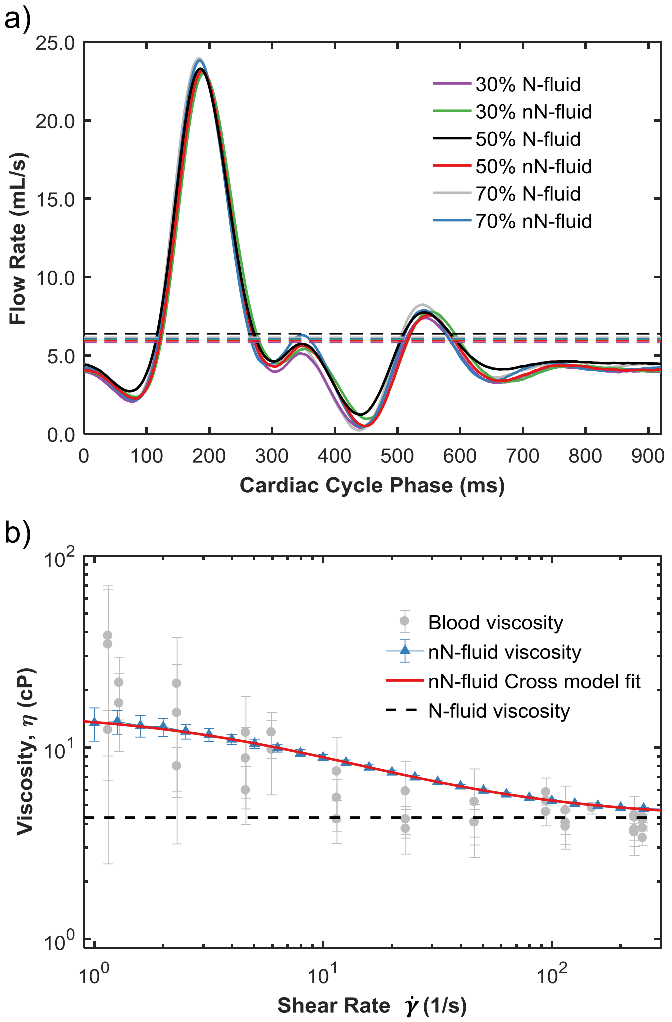

**Figure 2.** (a) Flow waveforms measured at the CCA inlet for each experimental PIV dataset (phase averaged from 15 cardiac cycles). Dashed lines represent the mean flow-rate in each case (6.1 ± 0.2 mL/s averaged across all models). (b) Experimental fluid viscosity versus shear rate. Blood data is taken from recent literature [36–41]. Solid line shows Cross model fit to non-Newtonian blood analogue fluid viscosity measurements. Dashed line indicates constant viscosity of Newtonian blood analogue fluid.

In the case of a shear-thinning fluid, the viscosity is dependent on the local magnitude of the shear rate, as described by the Cross model in Eq. (1). The deviatoric stress tensor formulation becomes

$$\boldsymbol{\tau} = \eta(\dot{\gamma})\dot{\boldsymbol{\gamma}} \tag{7}$$

The magnitude of the shear rate may be calculated from the second invariant of the rate-of-strain tensor as

$$\dot{\gamma} = \sqrt{\frac{1}{2}tr\left(\dot{\boldsymbol{\gamma}}^2\right)} = \sqrt{\frac{1}{2}\dot{\boldsymbol{\gamma}} : \dot{\boldsymbol{\gamma}}} \tag{8}$$

From each surface point, the first three points, spaced 0.3 mm apart along the inward normal, were obtained at which the surrounding velocity data were interpolated using cubic polynomials in a $6 \times 6 \times 6$ neighborhood, and the null velocity was assigned at the wall point. The wall shear calculation was facilitated by a rotation of the coordinate system to align the wall normal direction with the $z$-axis, consistent with magnetic resonance imaging studies of WSS [14,21,47]. The interpolated velocities were rotated into the new coordinate system, where the reduced deformation tensor derivatives were calculated. The transformed velocities were fit with a shape-preserving piecewise cubic polynomial, and the derivative of the fit at the wall location for each component was taken as the local shear rate in transformed coordinates. The WSS vector was taken as the local in-plane traction vector found from Eq. (6), and an inverse transformation was applied to obtain the WSS in real coordinates.

### 2.5.2. Calculation of wall shear parameters

Standard WSS parameters were derived for comparison across vessel geometries and viscosity models. The cycle average of the *magnitude* of the WSS vector, denoted time-averaged WSS (TAWSS), is defined as

$$\mathrm{TAWSS} = \frac{1}{T}\int_0^T |\boldsymbol{\tau_w}|dt \tag{9}$$

and the oscillatory shear index (OSI) as

$$\mathrm{OSI} = \frac{1}{2}\left[1 - \left(\frac{\left|\int_0^T \boldsymbol{\tau_w}dt\right|}{\int_0^T |\boldsymbol{\tau_w}|dt}\right)\right] = \frac{1}{2}\left[1 - \left(\frac{|\boldsymbol{\tau}_{\mathrm{mean}}|}{\mathrm{TAWSS}}\right)\right] \tag{10}$$

where the mean WSS vector is

$$\boldsymbol{\tau}_{\mathrm{mean}} = \frac{1}{T}\int_0^T \boldsymbol{\tau_w}dt \tag{11}$$

The transverse wall shear stress, defined by Peiffer et al. [7] as the time average of the component of WSS acting perpendicular to the direction of the mean WSS vector, is calculated as

$$\mathrm{transWSS} = \frac{1}{T}\int_0^T \left|\boldsymbol{\tau_w} \cdot \left(\boldsymbol{N} \times \frac{\int_0^T \boldsymbol{\tau_w}dt}{\left|\int_0^T \boldsymbol{\tau_w}dt\right|}\right)\right| \tag{12}$$

To quantify the spatial extent of cycle-averaged WSS parameters, a thresholding method was used, similar to that applied by others [48–50]. In this case, the 50% eccentric stenosis geometry with N-fluid is chosen as a reference from which threshold levels are calculated corresponding to the 20th percentile of the distribution for low TAWSS and the 80th percentile of the distribution of OSI and transWSS; this results in the following thresholds: $\mathrm{TAWSS}_{20} = 0.69$ Pa, $\mathrm{OSI}_{80} = 0.18$, $\mathrm{transWSS}_{80} = 0.51$ Pa. The surface area exposure to levels of the time-averaged parameters below the 20th percentile or exceeding the 80th percentile thresholds was calculated.

### 2.5.3. Turbulence intensity

Reynolds numbers were estimated from the mean axial velocity across central plane profiles and the corresponding vessel diameter as $Re = \rho VD/\mu$. Peak and cycle-mean Reynolds numbers in the CCA (averaged across all models) were 1502 and 523, respectively. For comparison, peak and cycle-mean Reynolds numbers calculated within the narrowest stenosis diameter were 1266 and 416 for the 30% model, 1611 and 533 for the 50% model, and 1786 and 724 in the 70% model.

The turbulence intensity (TI) metric was previously used to quantify disturbed flow in models of varying stenosis severity, plaque eccentricity and plaque ulceration using both ultrasound and PIV [35,51,52]. Turbulence intensity is calculated based on Reynold's decomposition method as

$$u'_i(t,n) = u_i(t,n) - U_i(t) \tag{13}$$

$$TI_i(t) = \sqrt{\frac{\sum_{n=1}^{N} u'_i(t,n)u'_i(t,n)}{N-1}}, \quad i = x, y, z \tag{14}$$

$$TI(t) = \sqrt{(TI_x(t))^2 + (TI_y(t))^2 + (TI_z(t))^2} \tag{15}$$

where $u'$ is the velocity fluctuation, and $U$ is the phase-averaged velocity for each component. The chosen number of cardiac cycles used in the TI estimation was $N = 15$, shown previously to be the minimum number of sequential cycles required for statistical convergence of the TI value [35].

To compare the evolution of turbulence intensity over time, TI values were averaged over a downstream region of interest (ROI) extending wall-to-wall and approximately one CCA diameter (8 mm) axially. The ROI location was selected as the region where ROI-averaged TI (denoted $\overline{\mathrm{TI}}$) reached a maximum, and only central-plane values were included in the mean calculation. Uncertainties in $\overline{\mathrm{TI}}$ were reported as the absolute maximum difference in $\overline{\mathrm{TI}}$ incurred when the ROI was shifted by ±4 mm, reflecting the sensitivity to the selection of the ROI location.

### *2.5.4. Uncertainty analysis*

PIV uncertainties were analyzed using commercial software (DaVis 8.4, LaVision Inc.) which utilizes the correlation statistics method [53]. Uncertainties were calculated for the 50% stenosed model with Newtonian fluid at peak systole ($t = 180$ ms) and at diastole for comparison ($t = 830$ ms). Uncertainties in the WSS are influenced by several factors, including velocity uncertainty and errors in the segmentation and registration of the CT surface. Given the complexity of the WSS calculation method, a Monte Carlo approach was taken to provide an estimate of the WSS uncertainty propagated from the spatial distribution of velocity errors and random 3D misalignments of the CT surface and velocity data. The WSS calculation was iterated 1000 times. The distribution of resulting velocity magnitude at each location was normal with mean equal to the measured velocity and standard deviation equal to the local uncertainty in velocity magnitude. Thus, vectors were limited to their original direction and only varied in magnitude. For each iteration, the registered CT surface was shifted up to one voxel (154 um) in a random direction uniformly distributed on the unit sphere. The standard deviation of the resulting WSS distribution at each surface point was used to estimate WSS uncertainty.

## 3. Results

### *3.1. Velocity and turbulence intensity*

Figure 3 shows the phase-averaged velocity magnitude in the central-plane slice ($z = 0$ mm) for the time point corresponding to peak systole ($t = 180$ ms). A high-velocity jet extends from the stenosis throat along the inner wall, eventually crossing through the lumen and impinging at the outer ICA wall before separating into two recirculation zones, indicated on Figure 3(c). Flow in the CCA and ECA is generally well organized and approximately laminar. Comparable maximum jet velocities were reached for N-fluid compared to nN-fluid with decreases of 6.9%, 0.02% and 0.56% in the absolute maximum velocities reached in the 30%, 50% and 70% geometries, respectively. The spatial coverage of velocities greater than the maximum scale limit was larger for the N-fluid as indicated by the black contours, and this effect was more pronounced for the 30% stenosed case.

Central-plane phase-averaged velocity profiles in the ICA are shown in Figure 4, displaying the centerline-projected velocity at peak systole for axial locations beginning in the recirculation zone and spaced 6 mm along the centerline, as indicated in the right panels of Figure 3 for each geometry. Velocity profiles for nN-fluid models appear blunted compared to N-fluid models. For S1 and S2, a slight deflection of the jet toward the flow-divider wall is evident for nN-fluid models, contributing to a steeper gradient and thus higher WSS at the inner wall. The temporal variation in velocity profiles is shown in Figure 5 for the 50% stenosed model. At S1, blunted jet-velocity profiles for the nN-fluid persist throughout the cardiac cycle including a shift of the maximum velocity towards the flow divider wall and slightly more flow reversal in the recirculation region (negative velocities at radial distance >1 mm). In the downstream region at S5, greater variation between N-fluid and nN-fluid profiles can be observed, reflective of the disturbed flow environment in this region.

Figure 6 shows central-plane TI maps in the ICA for the time point of maximum $\overline{\mathrm{TI}}$ for each model ($t = 180–200$ ms), which occurs in the deceleration portion of the cardiac cycle just after peak systole. The disturbed flow region extends from the inner wall across the lumen where the jet detaches and expands into the downstream ICA. A transverse slice is also shown at the center of the selected ROI, from which patterns are approximately symmetric about the central plane. Evolution of $\overline{\mathrm{TI}}$ over time is illustrated in Figure 7, with the selected ROIs indicated by rectangular boxes in Figure 6. TI values are summarized in Table 2. The peak $\overline{\mathrm{TI}}$ as well as the absolute single-site maximum TI values decreased for the nN-fluid compared to the N-fluid for 30% and 50% stenosis but increased for the 70% case. Although the peak $\overline{\mathrm{TI}}$ reached in the 70% stenosed model is higher for the nN-fluid compared to N-fluid, we see that high $\overline{\mathrm{TI}}$ values are sustained for a longer time frame for the N-fluid (Figure 7) resulting in a larger cycle-averaged $\overline{\mathrm{TI}}$ than the nN-fluid (Table 2).

Central plane ensemble averaged velocity uncertainties are shown in Supplementary Figure A1. The error in the ensemble average contains both the measurement errors and contributions due to velocity fluctuations [54,55]. The highest errors are found at locations with high shear gradients, such as at the boundaries of the high-velocity jet, propagated from the instantaneous velocity uncertainties. The contribution from flow fluctuations increases the uncertainties in the downstream ICA region due to the disturbed flow, as reflected by the TI metric. At peak systole in the 50% stenosed model with N-fluid, maximum uncertainties in the ensemble averaged velocity propagated from instantaneous velocity errors were approximately 0.09 m/s. When contributions from flow fluctuations were included, the maximum increased to 0.23 m/s and the overall average uncertainty was 0.06 m/s. The maximum and average overall uncertainties at diastole were 0.08 m/s and 0.03 m/s, respectively.

### *3.2. Wall shear stress and shear metrics*

Figure 8 shows the TAWSS for all phantoms. For 3D visualization purposes, the vessel is shown in two orientations exposing the inner and outer walls of the ICA on the left and right, respectively. The outer wall region, along the large recirculation zone, from the stenosis throat to the jet impingement site contains the lowest shear rates. A region of elevated TAWSS occurs at the stenosis throat and continues distally along the inner wall of the ICA adjacent to the high-velocity jet. Instantaneous WSS maps (not shown) showed qualitatively similar patterns. Absolute maximum WSS values (Table 3), occurring at peak systole for all models, were 22.9%, 9.6%, and 2.2% higher for the nN-fluid compared to N-fluid counterparts. N-fluid consistently underestimated WSS compared to nN-fluid when averages were taken over each of the vessel branches. WSS maps at peak systole are shown in Supplementary Figure A2.

WSS uncertainty maps for the 50% stenosed model with N-fluid at peak systole are shown in Supplementary Figure A3. Errors due to velocity fluctuations were not included in the WSS uncertainty maps shown, reflecting the propagation of only PIV measurement errors. Errors propagated from the registration step are dominant to errors propagated from uncertainty in velocity data. The average percentage error in WSS magnitude over all points was 14%,

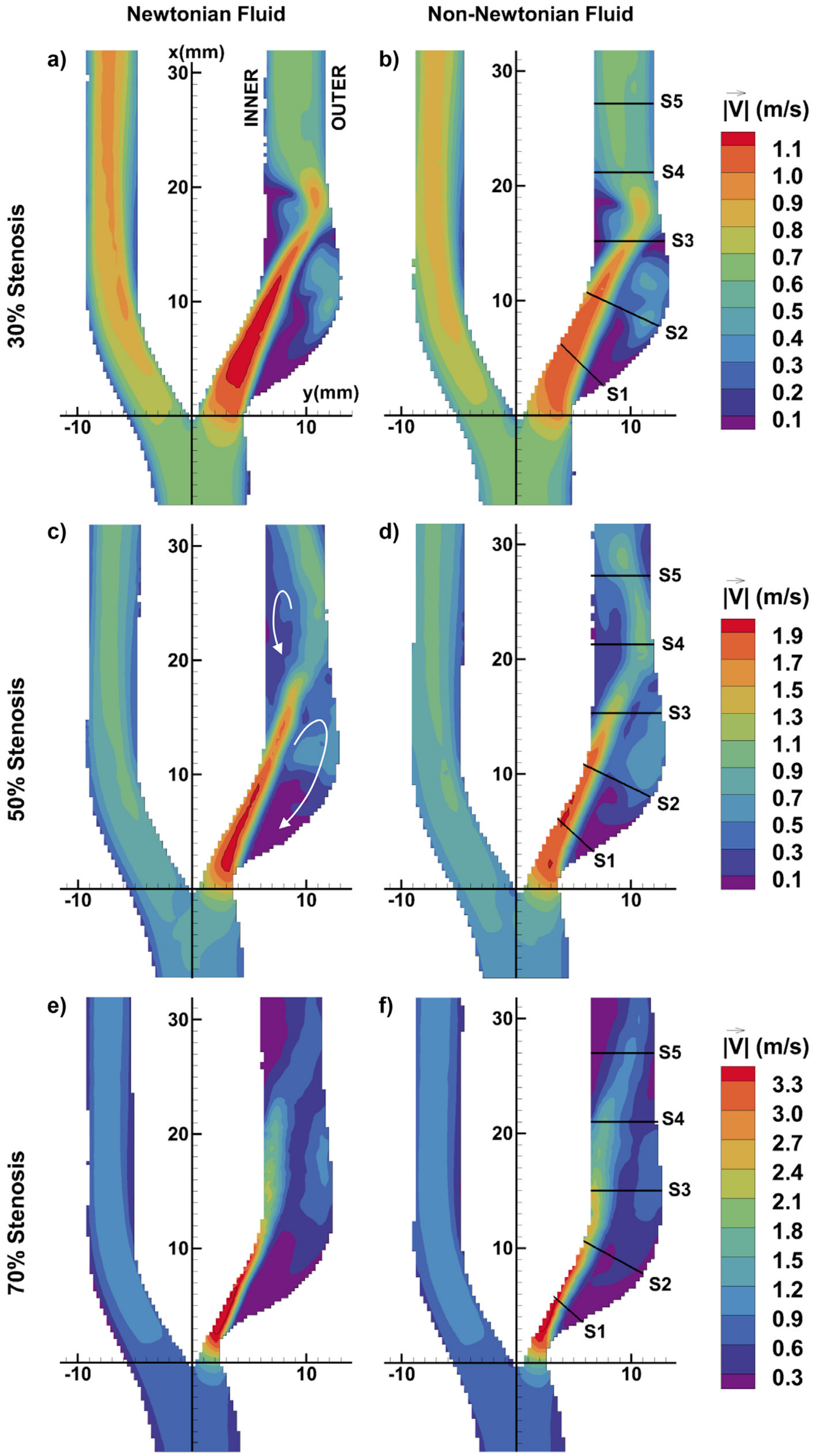

**Figure 3.** Central plane phase-averaged velocity magnitude at peak systole ($t = 180$ ms). Note that each row of models has an individual color bar. Contour lines correspond to the highest contour level in each row. Recirculation regions are indicated in white on panel c. Slices S1-S5 on panels a, d, and F indicate cross-sections where velocity profiles are extracted for each geometry.

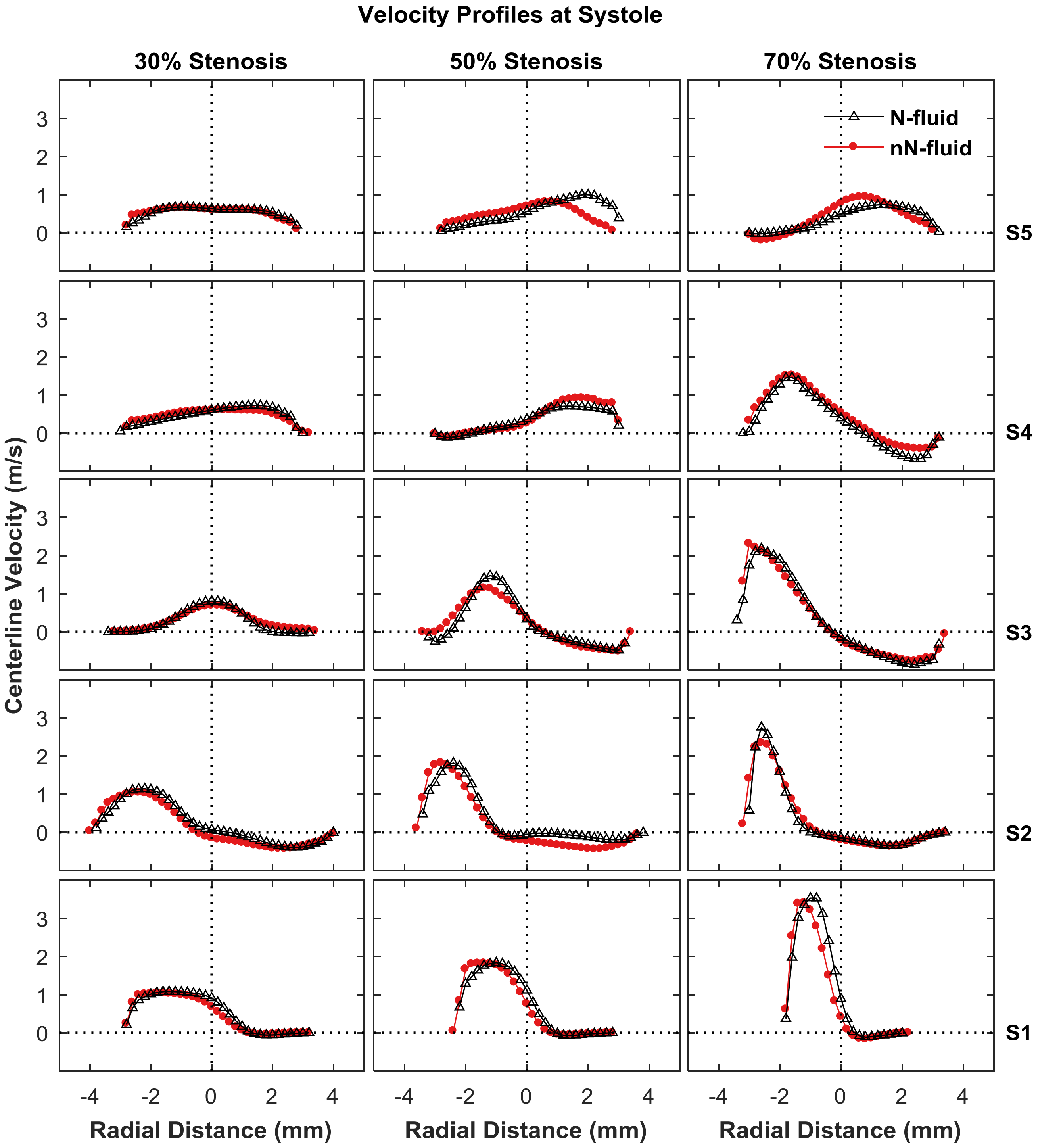

**Figure 4.** Phase-averaged centerline-projected velocity profiles at peak systole. Profiles are extracted from the central plane ICA at slices S1–S5 spaced 6 mm apart along the centerline indicated in Figure 3.

**Table 2**
Turbulence intensity parameters. Absolute max TI is the maximum single site TI value found within the ROI, indicated by the boxed area in Figure 6. Maximum $\overline{\text{TI}}$ refers to the peak ROI averaged TI value (at $t = 180 - 200$ ms) and cycle-averaged $\overline{\text{TI}}$ refers to the temporal and spatial mean over the ROI. Errors indicate the maximum differences incurred from shifting the ROI ±4 mm axially.

| Geometry | 30% stenosis | | 50% stenosis | | 70% stenosis | |
|---|---|---|---|---|---|---|
| | N-fluid | nN-fluid | N-fluid | nN-fluid | N-fluid | nN-fluid |
| Absolute max. TI (m/s) | 0.502 | 0.453 | 0.695 | 0.653 | 1.293 | 1.379 |
| Maximum $\overline{\text{TI}}$ (m/s) | 0.222 ± 0.054 | 0.204 ± 0.052 | 0.375 ± 0.064 | 0.320 ± 0.050 | 0.462 ± 0.041 | 0.493 ± 0.073 |
| Cycle-averaged $\overline{\text{TI}}$ (m/s) | 0.039 ± 0.006 | 0.033 ± 0.006 | 0.078 ± 0.012 | 0.073 ± 0.017 | 0.148 ± 0.036 | 0.140 ± 0.032 |

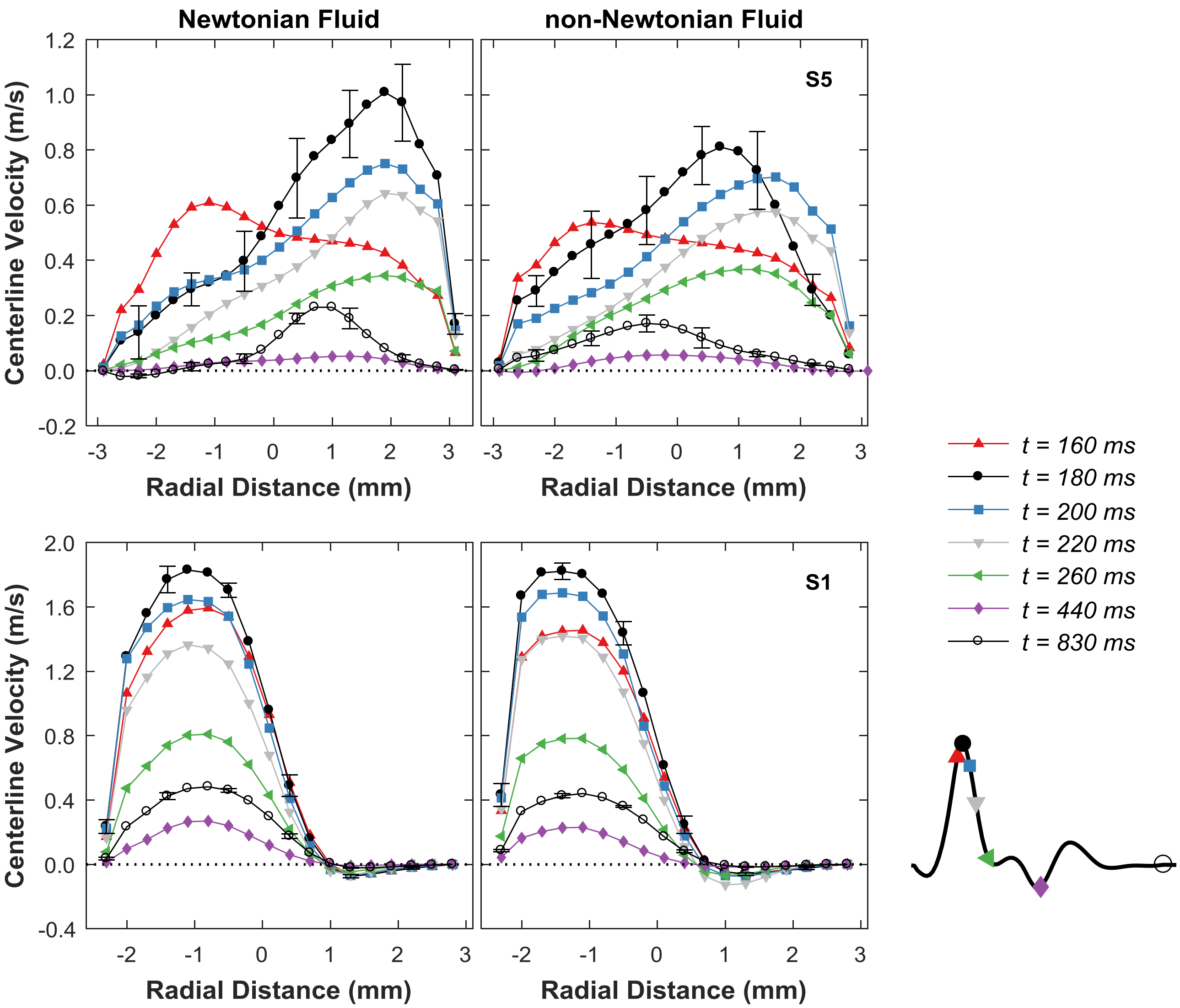

**Figure 5.** Temporal phase-averaged centerline-projected velocity profiles for the 50% eccentric geometry, extracted from the central plane ICA at slices S1 (bottom row) and S5 (top row) indicated in Figure 3. Sparse error bars representing standard deviation are shown for the profiles corresponding to peak systole and diastole.

**Table 3**
Wall shear stress parameters. Absolute max. WSS refers to the maximum single site WSS value. Remaining values are mean of the parameter over the specified vessel branch with standard deviation in parenthesis.

| Geometry | 30% stenosis | | 50% stenosis | | 70% stenosis | |
|---|---|---|---|---|---|---|
| | N-fluid | nN-fluid | N-fluid | nN-fluid | N-fluid | nN-fluid |
| Absolute max. WSS (Pa) | 20.75 | 25.49 | 41.92 | 45.94 | 88.24 | 90.22 |
| Absolute max. TAWSS (Pa) | 5.03 | 7.09 | 13.21 | 13.79 | 31.67 | 31.66 |
| TAWSS–CCA (Pa) | 0.73 (0.29) | 1.03 (0.35) | 0.96 (0.31) | 1.29 (0.31) | 1.12 (0.26) | 1.53 (0.39) |
| TAWSS–ICA (Pa) | 1.30 (0.99) | 1.93 (1.55) | 2.43 (2.45) | 2.84 (3.05) | 4.18 (6.12) | 4.57 (6.28) |
| TAWSS–ECA (Pa) | 1.29 (0.49) | 1.77 (0.64) | 1.42 (0.61) | 1.87 (0.58) | 1.50 (0.52) | 2.00 (0.51) |
| OSI–ICA | 0.09 (0.11) | 0.08 (0.12) | 0.09 (0.11) | 0.08 (0.10) | 0.10 (0.11) | 0.08 (0.09) |
| transWSS–ICA (Pa) | 0.22 (0.15) | 0.30 (0.20) | 0.35 (0.25) | 0.45 (0.34) | 0.53 (0.51) | 0.68 (0.62) |

however point-by-point relative errors vary considerably at systole due to the high dynamic range of velocities. For the highest WSS values (top 10%) the mean WSS and error was 26 ± 1 Pa. For the lowest WSS values (bottom 10%) the mean WSS and error was 1.0 ± 0.2 Pa. When flow fluctuations are included in the uncertainty propagation, the average error in WSS magnitude increases by approximately 10%. WSS uncertainty maps at diastole are shown in supplementary figure A4 in which absolute error values are lower, but WSS values are also much lower, resulting in a higher average relative error of 30%.

Figure 9 shows maps of the OSI computed from Eq. (10) overlayed with a sparse sample of unit vectors representing the direction only of the temporal mean WSS vector, $\tau_{\text{mean}}$ (Eq. (11)). Elevated OSI demarcates regions of flow impingement and recirculation, occurring in a ring pattern at the outer ICA wall and at the distal inner ICA wall. Insets in Figure 9 emphasize that elevated OSI tends to occur at, (1) sites of flow impingement and subsequent divergence of the mean WSS vector as in P1, P3 and P5 at the distal edge of recirculation zones, (2) sites where oppositely directed flow meet as in P4 where the jet flow meets with that

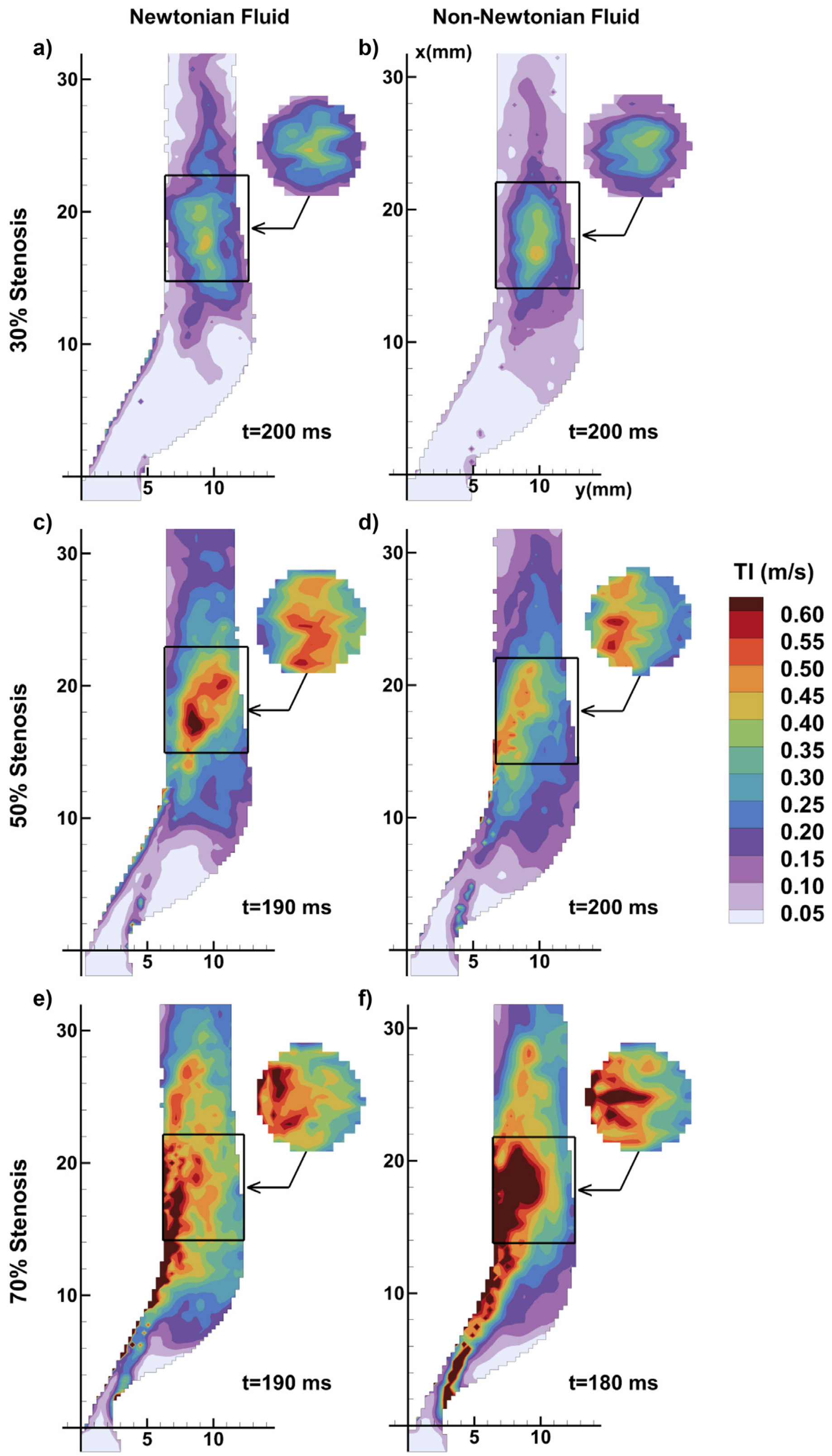

**Figure 6.** Central plane maps of turbulence intensity magnitude in the ICA, shown at the time point of peak ROI-averaged TI, as indicated in each panel. A transverse slice is shown for each model at the center of the ROI, which is indicated by the boxed area.

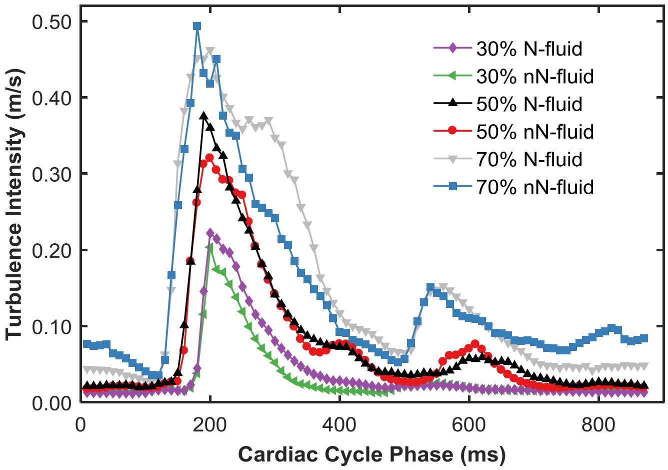

**Figure 7.** ROI-averaged TI versus cardiac cycle time for all models.

from the distal recirculation and also P3 where flow streams along the front and back of the ICA merge at the plane of symmetry, and (3) where a vortex occurs adjacent to the wall as in P2. Models with nN-fluid experience reduced OSI at the downstream inner ICA wall compared to N-fluid but slight increase in OSI levels and surface coverage in the outer ICA wall region.

Figure 10 shows elevated transWSS regions occur at the inner ICA adjacent to the jet, extending along the distal recirculation zone, and then at the jet impingement location on the outer ICA wall. Like TAWSS, absolute magnitude of transWSS increases with increasing stenosis severity and is noticeably increased for nN-fluid, reflective of the overall higher WSS magnitude for nN-fluid. If the transWSS at each surface point is normalized by the local TAWSS (shown in Supplementary Figure A5), the distributions are very similar to OSI maps, suggesting the low magnitude transverse WSS components may be captured with the OSI metric. However, the transWSS metric also includes regions with elevated transverse component due to small directional changes for high-shear flows, evident in the inner-wall region in Figure 10(f).

Finally, luminal surface exposure to time-averaged shear metrics is summarized in Figure 11. Surface area exposed to low shear magnitude, calculated as TAWSS$_{20}$, decreases with stenosis severity. N-fluid assumption leads to consistently underestimated WSS, thus area exposed to low shear is reduced with nN-fluid by 7.5%, 5.8%, and 8.4% compared to N-fluid counterparts. Fraction of surface area exposed to high OSI is comparable (~20% average) for all models (Figure 11, center) despite changes in location and pattern with disease progression and fluid type (Figure 8). OSI$_{80}$ appears suppressed in nN-fluid models, as is the mean OSI over the ICA (Table 3). The surface area exposed to high transWSS increases with increasing stenosis severity with additional increase in nN-fluid models compared to N-fluid, reflective of the area exposed to high shear magnitude in general. Lastly, differences in the surface area exposure between Newtonian and non-Newtonian fluids are most pronounced in the most severely stenosed 70% model, suggesting that the assumption of a Newtonian viscosity model will have the most impact in these cases.

## 4. Discussion

We have presented a method of estimating wall shear stress direction and magnitude in carotid artery models using a combination of PIV and CT and showed detailed maps of disturbed flow and WSS-based predictors with disease progression for varying degrees of eccentric stenosis and different blood analogue fluid types. The results demonstrate that a Newtonian fluid assumption underestimates the WSS magnitude, and thus also overestimates luminal surface exposure to sustained low WSS. The low-shear area decreases with increasing stenosis severity, since higher WSS is sustained with increasing jet velocity through the stenosis. The effect of viscosity model on shear stress patterns has been investigated in several numerical and experimental studies incorporating stenosed tubes or complex vascular geometries. Of these, some report higher WSS in Newtonian models [56,57] but most report higher WSS for non-Newtonian viscosity models [29,30,58–61]. However, others have demonstrated that for a given geometry the WSS measured depends upon the chosen non-Newtonian viscosity model [62–65] and that the effects of viscosity model can vary for different geometries [63]. Moreover, in computational studies of the carotid bifurcation under various rheological models, the calculation of WSS descriptors and bulk flow metrics were much less sensitive to blood rheology than the geometry reconstruction process [66,67]. However, we have demonstrated that the impact of rheology on exposure to low and oscillatory shear is more pronounced for higher levels of stenosis, indicating that sensitivity to rheology could change with the progression of vascular disease.

Despite the gaining popularity of OSI as a vascular disease metric, limited studies examine the impact of viscosity on the results of experimental and numerical simulations measuring oscillatory and complex flow. Overall, the N-fluid predicts higher OSI magnitude and surface exposure compared to the nN-fluid. OSI distributions indicate that regions of oscillatory wall shear are mostly governed by the presence and size of flow recirculation zones. High OSI appears due to temporal fluctuations in the sites of flow detachment and re-attachment, which bound regions of continuous flow reversal (recirculation), as shown by Razavi et al. [68] in a simple stenosis model. Other studies in a carotid bifurcation model [30] and in a straight vessel downstream of a wire stent [61] found only one OSI peak for non-Newtonian viscosity models, compared to the two observed for Newtonian when looking along a single dimension. Here we can see that as the second recirculation zone size increases with stenosis severity, an OSI hotspot (single peak axially) at the downstream flow impingement opens into a ring pattern (producing two peaks axially) as seen on the inner ICA wall when progressing from the 30–50% stenosis model in Figure 9(a)/(c). This effect is delayed for the nN-fluid, as a single OSI hotspot is still observed for the 50% stenosis with nN-fluid.

To our knowledge, this is the first study to look at the effects of shear thinning on transWSS. The present study demonstrates that the luminal surface area exposed to relatively high transWSS increases with stenosis severity and is underestimated by a Newtonian fluid model due to overall underestimation in WSS. TransWSS was first introduced by Peiffer et al. [7] as a new shear metric inspired by cell studies observing that endothelial cells responded to changes in flow direction perpendicular (transverse) to their axis of elongation [5]. High transWSS, as originally formulated by Peiffer, Ref. [7] can be indicative of either (1) large changes in flow direction, (2) small changes in direction over a long period of time, or (3) small changes in direction of high speed and high shear flow [7]. When the transWSS was normalized here by the site-specific TAWSS, we found that the regions experiencing the highest fractional transWSS were qualitatively similar to the high OSI regions, as shown in supplementary figure A5. However, when transWSS is not normalized, contributions from small side-to-side changes in direction within high speed flow regions, such as at the ICA inner wall jet region, contribute largely to the transWSS. This type of high-speed oscillatory near-wall flow may be more relevant when considering the risk of plaque rupture and thrombosis as stenosis severity increases, as opposed to plaque development often associated with low magnitude shear stress. A limited number of studies have investigated transWSS

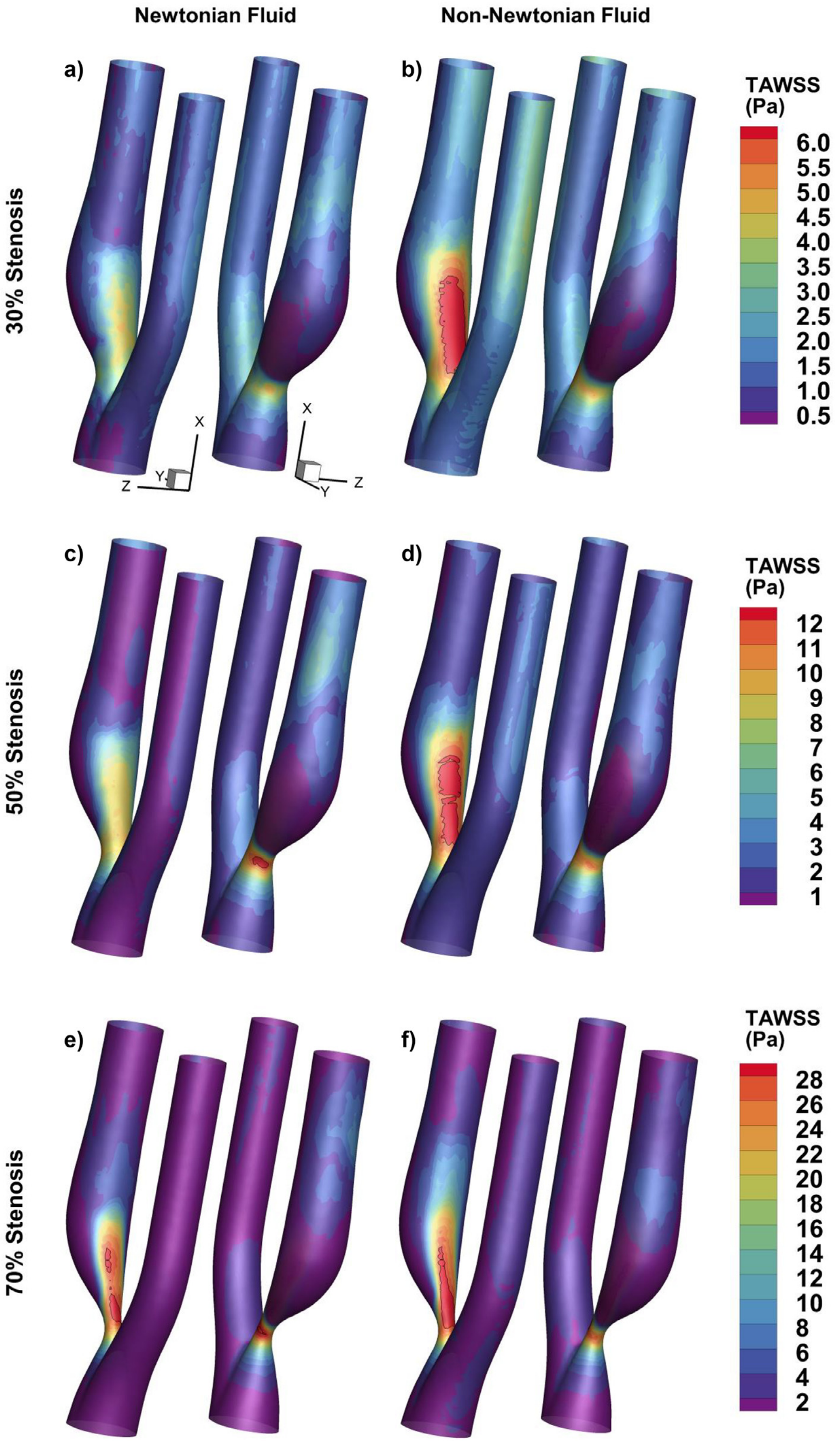

**Figure 8.** Contours of TAWSS. Each model is shown in two orientations, exposing the inner and outer walls of the ICA on the left and right, respectively. Note that each row of models has an individual color bar. Contour lines correspond to the highest contour level in each row.

using numerical simulations. Mohamied et al. [10] found that lesion prevalence correlated more strongly with transWSS than conventional OSI and TAWSS metrics in the rabbit aorta, supporting earlier qualitative observations by Peiffer [7]. Conversely, in a study of healthy human carotid bifurcations, Gallo et al. [69] observed that high transWSS was commonly located at the bifurcation apex, a site where lesions do not frequently occur. Further investigations will be necessary to determine the relevance of transWSS to the pathology of atherosclerosis.

The present study demonstrated that overall nN-fluid resulted in suppression of flow disturbances, in terms of peak value or temporal extent, resulting in a lower cumulative level of turbulence

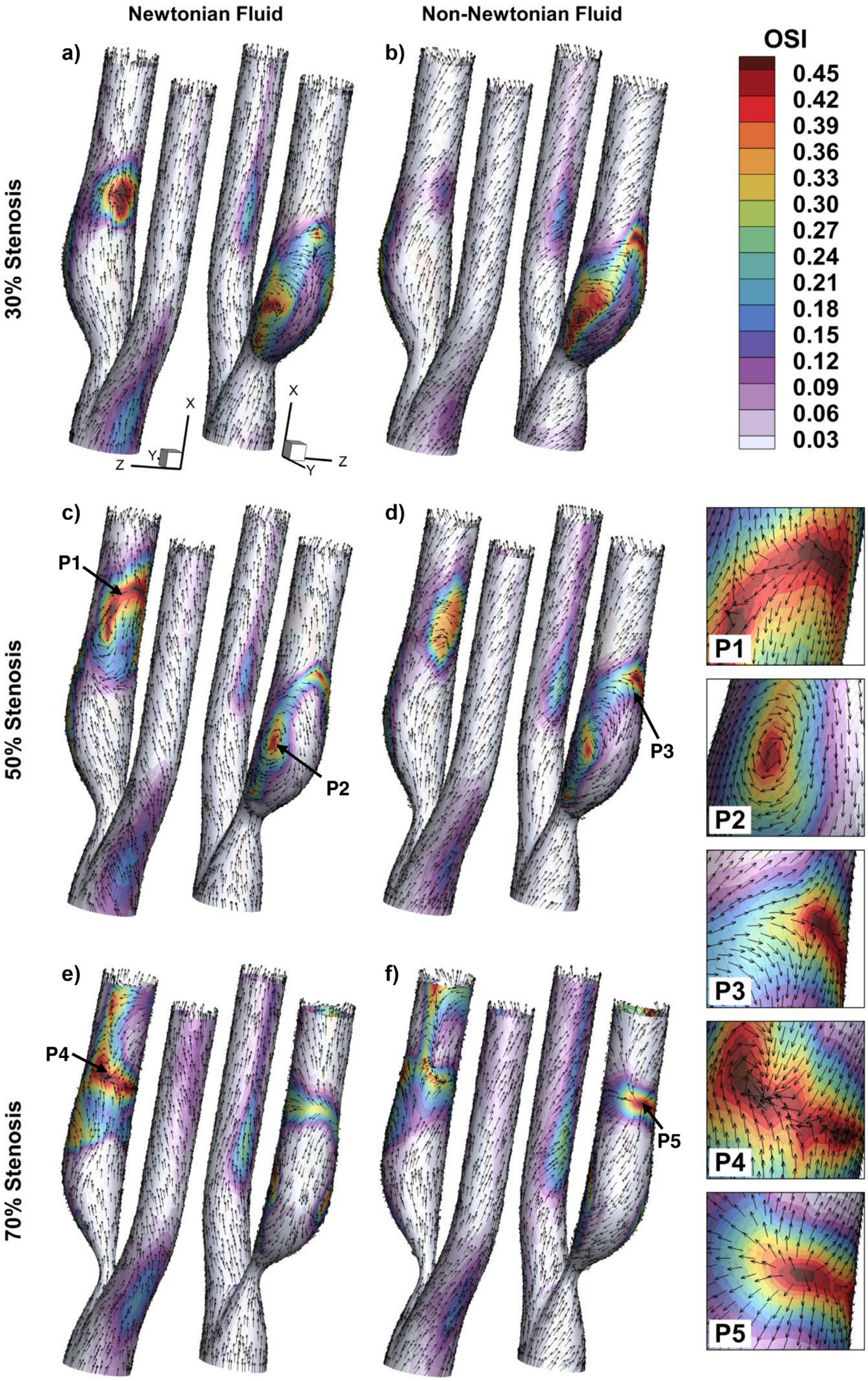

**Figure 9.** Contours of OSI overlayed with a sparse sample of unit vectors representing the direction only of the mean WSS vector. Each model is shown in two orientations, exposing the inner and outer walls of the ICA on the left and right, respectively. Insets provide enlarged views from points P1 through P5 whose locations are indicated in panels c-f depicting three key contributors to OSI: flow impingement on wall (P1, P3, P5), flow streams merging along wall (P3, P4), and wall-adjacent vortical flow (P2).

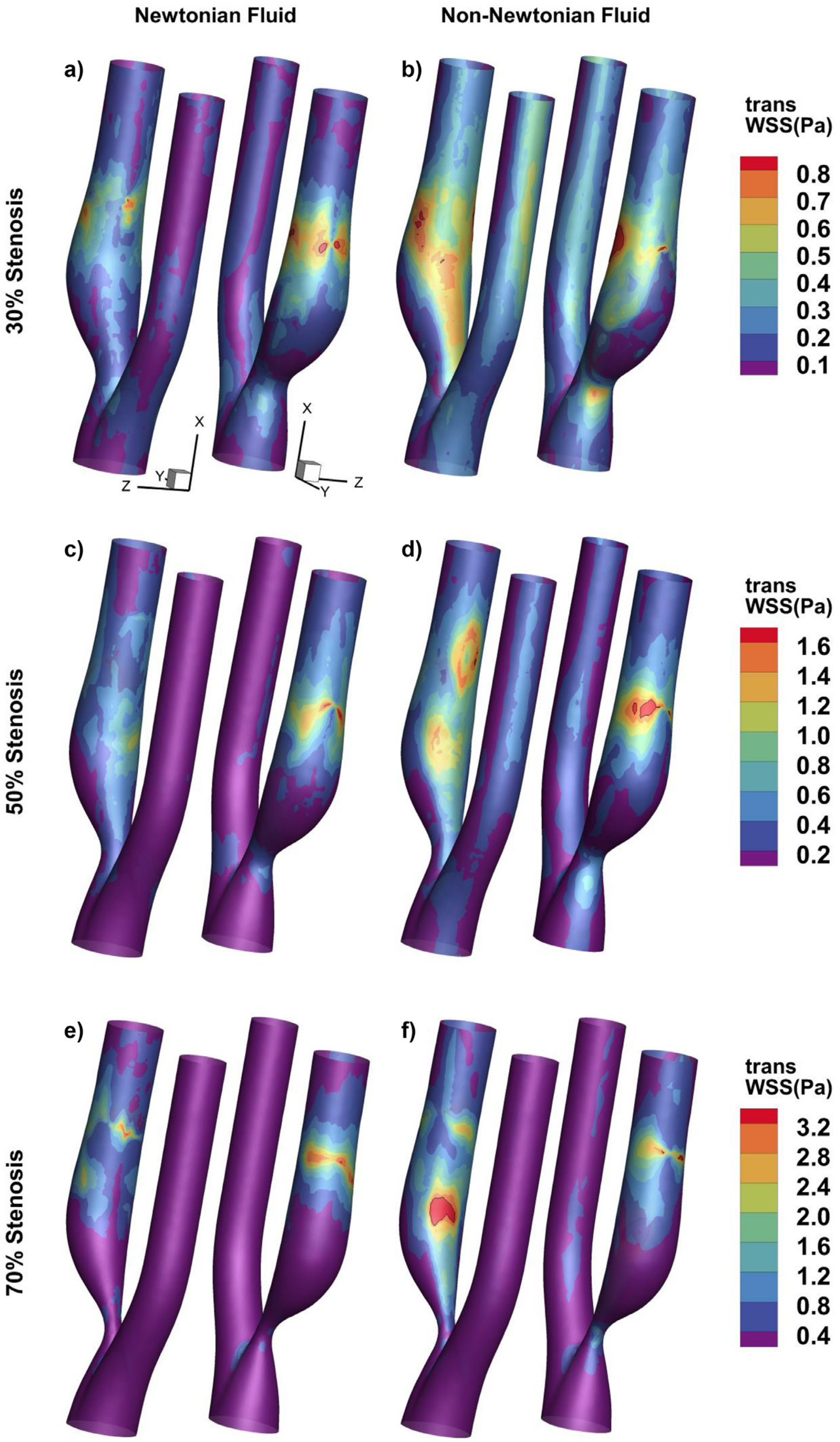

**Figure 10.** Contours of transWSS. Each model is shown in two orientations, exposing the inner and outer walls of the ICA on the left and right, respectively. Each row of models has an individual color bar and contour lines correspond to the highest contour level in each row.

intensity over the cardiac cycle. Only modest differences (0.02–0.06 m/s) in the $\overline{\text{TI}}$ metric were observed between viscosity models in matched geometries when compared with increases due to increases in stenosis severity (0.15–0.29 m/s) for a single fluid type. For comparison, previous DUS studies in the same models showed differences of 0.02–0.08 m/s in peak ROI-averaged TI due to ulcerations [51,52] and previous PIV studies observed differences of 0.05–0.10 m/s in maximum ROI-averaged TI due to plaque eccentricity [35]. Molla and Paul [60] observed that the turbulent kinetic energy (TKE) downstream of a simple 50% stenosis was higher for a Newtonian viscosity model compared to several non-Newtonian models, in line with the present result, and that high TKE persisted

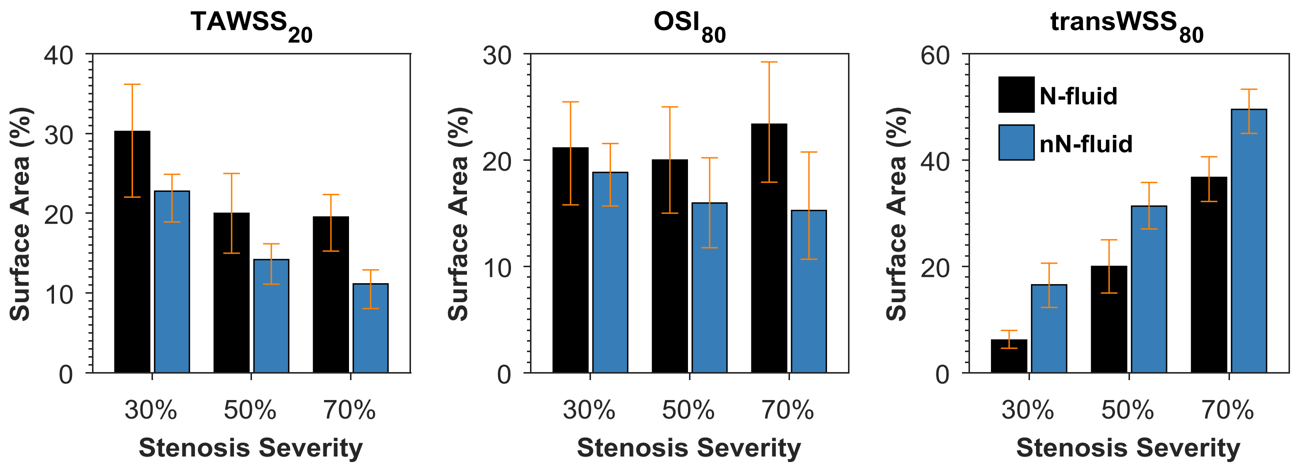

**Figure 11.** Surface area exposure as a function of stenosis severity and compared for Newtonian and non-Newtonian fluids. Values are ICA SA exposed to: TAWSS below, OSI above, and transWSS above the respective thresholds. Thresholds defined as the 20th, 80th and 80th percentile values, respectively, of the parameter on the 50% N-fluid ICA surface. Whiskers represent ICA SA coverage when the +/−5 percentile thresholds are applied.

further downstream for nN-fluid models compared to the N-fluid. Walker et al. [61] observed the turbulent Reynold's shear stress downstream of a stent to be up to 60% higher for a N-fluid compared to a nN-fluid but found that doubling the flow Reynold's number caused an increase in RSS for both models and additionally increased nN-fluid RSS to match that of the N-fluid. Similar to the effect seen here at higher stenosis, for a higher Reynold's number flow the maximum turbulence intensity is less dependent on the viscosity model.

A limitation of the present study is that the stereoscopic PIV technique requires the stacking of several independent planes of phase-averaged velocity data and a coherent instantaneous volumetric velocity field is not obtained. Thus, instantaneous WSS, and subsequently cycle-to-cycle temporal fluctuations in WSS, cannot be observed. Applying a tomographic PIV technique would overcome this issue, as previously explored by Buchmann et al. [26], but for wall shear magnitude only. The carotid models utilized here do not include physiological compliance. Numerical studies of the combined effect of non-Newtonian viscosity and compliance have shown that they can be interrelated, but in general, compliance has little effect on hemodynamic wall parameters [70]. While the phantoms utilized incorporate an idealized vessel geometry lacking tortuosity or vessel wall roughness, the matched set allows a controlled study of disease progression independent of additional factors.

The wall shear stress estimation can depend on the fitting technique and interpolation spacing applied to the discrete velocity data. Previous studies in the current geometries applied a central differencing scheme to calculate WSS magnitude for N-fluid [27]. While this method allowed a robust comparison between matched geometry models, it provided a conservative underestimate of WSS magnitude. In a study of wall shear rates derived from laser doppler anemometry measurements in a straight tube and different curve-fitting techniques, Fatemi and Rittgers [71] concluded that a third-degree polynomial curve fit with four points provided the most accurate shear-rate estimation for pulsatile flows in a straight tube. However, physiological flows are much more complex and have spatially varying boundary layer thickness and flow regimes. In the present case, a cubic polynomial curve fit with an interpolation spacing of 0.3 mm approximately equal to the in-plane velocity vector spacing was applied to ensure that interpolated points were within the first non-zero velocity from the wall and to ensure that interpolation points fall in unique and neighboring voxels where possible. The calculated systolic and time-averaged wall shear stress maps agree well with previous CFD studies for the 30% eccentrically stenosed geometry [72]. In that study, WSS values at peak systole reached 200 dyne/cm$^2$ (20 Pa) in the stenosis throat, and TAWSS reached 50 dyne/cm$^2$ (5 Pa) at the ICA inner wall and in the throat, similar to the values reported here for the 30% stenosed N-fluid model in Table 3 and Figure 8(a).

In conclusion, we have presented an experimental technique incorporating PIV velocity data and micro-CT geometry reconstruction resulting in both flow and multidirectional WSS parameters in addition to TI. We observed decreased $\text{TAWSS}_{20}$, comparable $\text{OSI}_{80}$ and increased $\text{transWSS}_{80}$, as well as increased TI, with increasing stenosis severity. In general, we found that shear stress may be underestimated, and disturbed flow may be exaggerated when shear thinning effects are neglected with the use of a N-fluid model. In addition, higher grades of stenosis exhibited larger differences in measured exposure to low and oscillatory shear between the fluid models. Thus, the importance of rheology may be specific to the level of disease progression, and studies investigating the impact of rheology on hemodynamics should include a range of geometries comprising various levels of flow disturbances.

## Conflict of interest

No conflicts of interest to disclose.

## Acknowledgments

The authors acknowledge Hristo Nikolov for phantom fabrication, Brian Dalrymple and Frank Van Sas for machining and technical help, Jaques Milner for segmentation and registration expertise, Joseph Umoh for assistance with CT scans and reconstruction, and Cameron Hopkins for rheometer data. Financial support is acknowledged from the Canada Foundation for Innovation (PIV system) and Ontario Ministry of Research and Innovation (PIV system, Early Researcher Award), Heart and Stroke Foundation of Ontario (operating grant #T-6427), Natural Sciences and Engineering Research Council of Canada (Discovery Grant), and Canadian Institutes of Health Research (FDN 148474). A. DiCarlo was partially supported by a Canadian Institutes of Health Research Training Fellowship in Vascular Research. D.W.H. is the Dr. Sandy Kirkley Chair of Musculoskeletal Research in the Schulich School of Medicine and Dentistry.

## Supplementary material

Supplementary material associated with this article can be found, in the online version, at doi:10.1016/j.medengphy.2018.12.023.

## References

[1] Morbiducci U, Kok AM, Kwak BR, Stone PH, Steinman DA, Wentzel JJ. Atherosclerosis at arterial bifurcations: evidence for the role of haemodynamics and geometry. Thromb Haemost 2016;115:484–92.
[2] Zarins CK, Giddens DP, Bharadvaj BK, Sottiurai VS, Mabon RF, Glagov S. Carotid bifurcation atherosclerosis quantitative correlation of plaque localization with flow velocity profiles and wall shear-stress. CircRes 1983;53:502–14.
[3] Caro CG, Fitzgera JM, Schroter RC. Atheroma and arterial wall shear – observation, correlation and proposal of a shear dependent mass transfer mechanism for altherogenesis. Proc R Soc Ser B Biol Sci 1971;177 pp. 109–+.
[4] Wentzel JJ, Chatzizisis YS, Gijsen FJH, Giannoglou GD, Feldman CL, Stone PH. Endothelial shear stress in the evolution of coronary atherosclerotic plaque and vascular remodelling: current understanding and remaining questions. Cardiovasc Res 2012;96:234–43.
[5] Wang C, Baker BM, Chen CS, Schwartz MA. Endothelial cell sensing of flow direction. Arterioscler Thromb Vasc Biol 2013;33:2130–6.
[6] Chakraborty A, Chakraborty S, Jala VR, Thomas JM, Sharp MK, Berson RE, et al. Impact of bi-axial shear on atherogenic gene expression by endothelial cells. Ann Biomed Eng 2016;44:3032–45.
[7] Peiffer V, Sherwin SJ, Weinberg PD. Computation in the rabbit aorta of a new metric – the transverse wall shear stress – to quantify the multidirectional character of disturbed blood flow. J Biomech 2013;46:2651–8.
[8] Ku DN, Giddens DP, Zarins CK, Glagov S. Pulsatile flow and atherosclerosis in the human carotid bifurcation – positive correlation between plaque location and low and oscillating shear-stress. Arteriosclerosis 1985;5:293–302.
[9] Peiffer V, Sherwin SJ, Weinberg PD. Does low and oscillatory wall shear stress correlate spatially with early atherosclerosis? A systematic review. Cardiovasc Res 2013;99:242–50.
[10] Mohamied Y, Rowland EM, Bailey EL, Sherwin SJ, Schwartz MA, Weinberg PD. Change of direction in the biomechanics of atherosclerosis. Ann Biomed Eng 2015;43:16–25.
[11] Morbiducci U, Gallo D, Cristofanelli S, Ponzini R, Deriu MA, Rizzo G, et al. A rational approach to defining principal axes of multidirectional wall shear stress in realistic vascular geometries, with application to the study of the influence of helical flow on wall shear stress directionality in aorta. J Biomech 2015;48:899–906.
[12] Arzani A, Shadden SC. Characterizations and correlations of wall shear stress in aneurysmal flow. J Biomech Eng Trans ASME 2016;138:10.
[13] Mohamied Y, Sherwin SJ, Weinberg PD. Understanding the fluid mechanics behind transverse wall shear stress. J Biomech 2017;50:102–9.
[14] van Ooij P, Potters WV, Nederveen AJ, Allen BD, Collins J, Carr J, et al. A methodology to detect abnormal relative wall shear stress on the full surface of the thoracic aorta using four-dimensional flow MRI. Magn Reson Med 2015;73:1216–27.
[15] Bieging ET, Frydrychowicz A, Wentland A, Landgraf BR, Johnson KM, Wieben O, et al. In vivo three-dimensional MR wall shear stress estimation in ascending aortic dilatation. J Magn Reson Imag 2011;33:589–97.
[16] Boussel L, Rayz V, Martin A, Acevedo-Bolton G, Lawton MT, Higashida R, et al. Phase-contrast magnetic resonance imaging measurements in intracranial aneurysms in vivo of flow patterns, velocity fields, and wall shear stress: comparison with computational fluid dynamics. Magn Reson Med 2009;61:409–17.
[17] Oyre S, Ringgaard S, Kozerke S, Paaske WP, Erlandsen M, Boesiger P, et al. Accurate noninvasive quantitation of blood flow, cross-sectional lumen vessel area and wall shear stress by three-dimensional paraboloid modeling of magnetic resonance imaging velocity data. J Am Coll Cardiol 1998;32:128–34.
[18] Isoda H, Ohkura Y, Kosugi T, Hirano M, Alley MT, Bammer R, et al. Comparison of hemodynamics of intracranial aneurysms between MR fluid dynamics using 3D cine phase-contrast MRI and MR-based computational fluid dynamics. Neuroradiology 2010;52:913–20.
[19] Frydrychowicz A, Stalder AF, Russe MF, Bock J, Bauer S, Harloff A, et al. Three--dimensional analysis of segmental wall shear stress in the aorta by flow-sensitive four-dimensional-MRI. J Magn Reson Imag 2009;30:77–84.
[20] Harloff A, Nussbaumer A, Bauer S, Stalder AF, Frydrychowicz A, Weiller C, et al. In vivo assessment of wall shear stress in the atherosclerotic aorta using flow-sensitive 4D MRI. Magn Reson Med 2010;63:1529–36.
[21] Stalder AF, Russe MF, Frydrychowicz A, Bock J, Hennig J, Markl M. Quantitative 2D and 3D phase contrast MRI: optimized analysis of blood flow and vessel wall parameters. Magn Reson Med 2008;60:1218–31.
[22] Petersson S, Dyverfeldt P, Ebbers T. Assessment of the accuracy of MRI wall shear stress estimation using numerical simulations. J Magn Reson Imag 2012;36:128–38.
[23] Brunette J, Mongrain R, Laurier J, Galaz R, Tardif JC. 3D flow study in a mildly stenotic coronary artery phantom using a whole volume PIV method. Med Eng Phys 2008;30:1193–200.
[24] Pielhop K, Klaas M, Schroder W. Analysis of the unsteady flow in an elastic stenotic vessel. Eur J Mech B Fluids 2012;35:102–10.
[25] Buchmann NA, Jermy MCASME. In-vitro blood flow and wall shear stress measurements in idealised and patient specific models of the carotid artery bifurcation. New York: Amer Soc Mechanical Engineers; 2009.
[26] Buchmann NA, Atkinson C, Jeremy MC, Soria J. Tomographic particle image velocimetry investigation of the flow in a modeled human carotid artery bifurcation. Exp Fluids 2011;50:1131–51.
[27] Kefayati S, Milner JS, Holdsworth DW, Poepping TL. In vitro shear stress measurements using particle image velocimetry in diseased carotid artery models: effect of stenosis severity, plaque eccentricity, and ulceration. PLoS One 2014;9:e98209.
[28] Huh HK, Ha H, Lee SJ. Effect of non-Newtonian viscosity on the fluid-dynamic characteristics in stenotic vessels. Exp Fluids 2015;56:12.
[29] Chen J, Lu XY. Numerical investigation of the non-Newtonian blood flow in a bifurcation model with a non-planar branch. J Biomech 2004;37:1899–911.
[30] Chen J, Lu XY. Numerical investigation of the non-Newtonian pulsatile blood flow in a bifurcation model with a non-planar branch. J Biomech 2006; 39:818–32.
[31] Fortais A, de Bruyn JR, Poepping TL. Non-Newtonian blood-mimicking fluid for particle image velocimetry. In: Proceedings of Canadian Congress of Applied Mechanics, London, Canada; 2015.
[32] Smith RF, Rutt BK, Holdsworth DW. Anthropomorphic carotid bifurcation phantom for MRI applications. J Magn Reson Imag 1999;10:533–44.
[33] Poepping TL, Nikolov HN, Rankin RN, Lee M, Holdsworth DW. An in vitro system for Doppler ultrasound flow studies in the stenosed carotid artery bifurcation. Ultras Med Biol 2002;28:495–506.
[34] Kefayati S, Poepping TL. Transitional flow analysis in the carotid artery bifurcation by proper orthogonal decomposition and particle image velocimetry. Med Eng Phys 2013;35:898–909.
[35] Kefayati S, Holdsworth DW, Poepping TL. Turbulence intensity measurements using particle image velocimetry in diseased carotid artery models: effect of stenosis severity, plaque eccentricity, and ulceration. J Biomech 2014; 47:253–63.
[36] Smith RF, Rutt BK, Fox AJ, Rankin RN, Holdsworth DW. Geometric characterization of stenosed human carotid arteries. Acad Radiol 1996;3:898–911.
[37] Fox AJ. Carotid endartectomy trials. Neuroimag Clin N Am. 1996;6:931–8.
[38] Holdsworth DW, Norley CJ, Frayne R, Steinman DA, Rutt BK. Characterization of common carotid artery blood-flow waveforms in normal human subjects. Physiol Meas 1999;20:219–40.
[39] Yousif MY, Holdsworth DW, Poepping TL. A blood-mimicking fluid for particle image velocimetry with silicone vascular models. Exp Fluids 2011; 50:769–74.
[40] Antonova N, Zvetkova E, Ivanov I, Savov Y. Hemorheological changes and characteristic parameters derived from whole blood viscometry in chronic heroin addicts. Clin Hemorheol Microcirc 2008;39:53–61.
[41] Bor-Kucukatay M, Keskin A, Akdam H, Kabuku-Hacioglu S, Erken G, Atsak P, et al. Effect of thrombocytapheresis on blood rheology in healthy donors: role of nitric oxide. Transfus Apher Sci 2008;39:101–8.
[42] Carrera LI, Etchepare R, D'Arrigo M, Vaira SM, Valverde J, D'Ottavio AE, et al. Hemorheologic changes in type 2 diabetic patients with microangiopathic skin lesions. A linear discriminant categorizing analysis. J Diabetes Compl 2008;22:132–6.
[43] Fehr M, Galliard-Grigioni KS, Reinhart WH. Influence of acute alcohol exposure on hemorheological parameters and platelet function in vivo and in vitro. Clin Hemorheol Microcirc 2008;39:351–8.
[44] Galduroz JCF, Antunes HK, Santos RF. Gender- and age-related variations in blood viscosity in normal volunteers: a study of the effects of extract of Allium sativum and Ginkgo biloba. Phytomedicine 2007;14:447–51.
[45] Vaya A, Murado J, Santaolaria M, Simo M, Mico L, Calvo J, et al. Haemorheological changes in patients with systemic lupus erythematosus do not seem to be related to thrombotic events. Clin Hemorheol Microcirc 2008;38:23–9.
[46] Antiga L, Piccinelli M, Botti L, Ene-Iordache B, Remuzzi A, Steinman D. An image-based modeling framework for patient-specific computational hemodynamics. Med Biol Eng Comput 2008;46:1097–112.
[47] Potters WV, van Ooij P, Marquering H, vanBavel E, Nederveen AJ. Volumetric arterial wall shear stress calculation based on cine phase contrast MRI. J Magn Reson Imag 2015;41:505–16.
[48] Lee SW, Antiga L, Spence JD, Steinman DA. Geometry of the carotid bifurcation predicts its exposure to disturbed flow. Stroke 2008;39:2341–7.
[49] Lee SW, Antiga L, Steinman DA. Correlations among indicators of disturbed flow at the normal carotid bifurcation. J Biomech Eng Trans ASME 2009; 131:7.
[50] Gallo D, Steinman DA, Bijari PB, Morbiducci U. Helical flow in carotid bifurcation as surrogate marker of exposure to disturbed shear. J Biomech 2012;45:2398–404.
[51] Wong EY, Nikolov HN, Thorne ML, Poepping TL, Rankin RN, Holdsworth DW. Clinical Doppler ultrasound for the assessment of plaque ulceration in the stenosed carotid bifurcation by detection of distal turbulence intensity: a matched model study. Eur Radiol 2009;19:2739–49.
[52] Wong EY, Nikolov HN, Rankin RN, Holdsworth DW, Poepping TL. Evaluation of distal turbulence intensity for the detection of both plaque ulceration and stenosis grade in the carotid bifurcation using clinical Doppler ultrasound. Eur Radiol 2013;23:1720–8.
[53] Wieneke B. PIV uncertainty quantification from correlation statistics. Meas Sci Technol 2015;26:10.
[54] Sciacchitano A, Wieneke B. PIV uncertainty propagation. Meas Sci Technol 2016;27:16.

[55] Wilson BM, Smith BL. Taylor-series and Monte-Carlo-method uncertainty estimation of the width of a probability distribution based on varying bias and random error. Meas Sci Technol 2013;24:11.
[56] Tu C, Deville M. Pulsatile flow of non-newtonian fluids through arterial stenoses. J Biomech 1996;29:899–908.
[57] Deplano V, Knapp Y, Bailly L, Bertrand E. Flow of a blood analogue fluid in a compliant abdominal aortic aneurysm model: experimental modelling. J Biomech 2014;47:1262–9.
[58] Ballyk PD, Steinman DA, Ethier CR. Simulation of non-newtonian blood-flow in an end-to-side anastomosis. Biorheology 1994;31:565–86.
[59] Luo XY, Kuang ZB. Non-Newtonian flow patterns associated with an arterial-stenosis. J Biomech Eng Trans ASME 1992;114:512–14.
[60] Molla MM, Paul MC. LES of non-Newtonian physiological blood flow in a model of arterial stenosis. Med Eng Phys 2012;34:1079–87.
[61] Walker AM, Johnston CR, Rival DE. The quantification of hemodynamic parameters downstream of a gianturco zenith stent wire using Newtonian and non-Newtonian analog fluids in a pulsatile flow environment. J Biomech Eng Trans ASME 2012;134:10.
[62] Caballero AD, Lain S. Numerical simulation of non-Newtonian blood flow dynamics in human thoracic aorta. Comput Methods Biomech Biomed Eng 2015;18:1200–16.
[63] Evju O, Valen-Sendstad K, Mardal KA. A study of wall shear stress in 12 aneurysms with respect to different viscosity models and flow conditions. J Biomech 2013;46:2802–8.
[64] Johnston BM, Johnston PR, Corney S, Kilpatrick D. Non-Newtonian blood flow in human right coronary arteries: steady state simulations. J Biomech 2004;37:709–20.
[65] Johnston BM, Johnston PR, Corney S, Kilpatrick D. Non-Newtonian blood flow in human right coronary arteries: transient simulations. J Biomech 2006;39:1116–28.
[66] Morbiducci U, Gallo D, Massai D, Ponzini R, Deriu MA, Antiga L, et al. On the importance of blood rheology for bulk flow in hemodynamic models of the carotid bifurcation. J Biomech 2011;44:2427–38.
[67] Lee SW, Steinman DA. On the relative importance of rheology for image-based CFD models of the carotid bifurcation. J Biomech Eng 2007;129:273–8.
[68] Razavi A, Shirani E, Sadeghi MR. Numerical simulation of blood pulsatile flow in a stenosed carotid artery using different rheological models. J Biomech 2011;44:2021–30.
[69] Gallo D, Steinman DA, Morbiducci U. Insights into the co-localization of magnitude-based versus direction-based indicators of disturbed shear at the carotid bifurcation. J Biomech 2016;49:2413–19.
[70] Kabinejadian F, Ghista DN. Compliant model of a coupled sequential coronary arterial bypass graft: effects of vessel wall elasticity and non-Newtonian rheology on blood flow regime and hemodynamic parameters distribution. Med Eng Phys 2012;34:860–72.
[71] Fatemi RS, Rittgers SE. Derivation of sheer rates from near-wall LDA measurements under steady and pulsatile flow conditions. J Biomech Eng Trans ASME 1994;116:361–8.
[72] Steinman DA, Poepping TL, Tambasco M, Rankin RN, Holdsworth DW. Flow patterns at the stenosed carotid bifurcation: effect of concentric versus eccentric stenosis. Ann Biomed Eng 2000;28:415–23.